







Cite this: *J. Mater. Chem. A*, 2024, 12, 979

# Counterion chemistry of 5-halo (X: Cl, Br, I)-uracil derived carbon nitride: unlocking enhanced photocatalytic performance†

Toshali Bhojar, <sup>a</sup> B. Moses Abraham, <sup>b</sup> Akanksha Gupta,<sup>c</sup> Dong Jin Kim,<sup>d</sup> Nilesh R. Manwar, <sup>e</sup> Kedhareswara Sairam Pasupuleti, <sup>f</sup> Devthade Vidyasagar <sup>\*ag<sup>h</sup></sup> and Suresh S. Umare <sup>\*a</sup>

The performance of modified polymeric carbon nitride (PCN) photocatalysts exceeds that of their bulk counterparts, owing to their distinct advantages and enhanced features. In this work, we present the synthesis methodology for halide-molecular doped PCN through a single molecule precursor approach by combining  $\pi$ -aromatic uracil and halide as a dopant and counterions, respectively. We systematically investigated the effect of halide ions ( $X^-$ :  $Cl^-$ ,  $Br^-$ , and  $I^-$ ) on the photoactivity of 5-halouracil derived PCN (XUCN). Our results demonstrate that halide counterions significantly enhance the photocatalytic activity of XUCN for hydrogen peroxide and hydrogen production ( $126.6 \mu\text{mol h}^{-1}$  and  $0.563 \text{ mmol h}^{-1} \text{ g}^{-1}$ ), compared to the undoped bulk PCN ( $48.3 \mu\text{mol h}^{-1}$  and  $0.260 \text{ mmol h}^{-1} \text{ g}^{-1}$ ). The charge-carrier analysis and structural analysis of synthesized XUCN catalysts suggest that the improvement in photoactivity is due to the synergistic interactions of uracil and halide ions, which enhance the charge-carrier lifetime (1.51 to 3.08 ns), generate additional catalytic sites ( $10.6$  to  $83.3 \text{ m}^2 \text{ g}^{-1}$ ), and extend light absorption (450 to 480 nm). Theoretical investigations reveal high structural stability for XUCN with favourable adsorption energies to bind with reactive oxygen species. The new insights provided in this study can have important implications for future design and synthesis of metal-free PCN with improved photoactivity *via* single molecule precursor doping.

Received 17th August 2023  
Accepted 28th November 2023

DOI: 10.1039/d3ta04938h

rsc.li/materials-a

## Introduction

Polymeric carbon nitride (PCN) is a promising metal-free photocatalyst for numerous solar-powered energy and environmental applications, due to its ideal bandgap and attractive physicochemical features.<sup>1–3</sup> However, the inherent limitations of bulk PCN-based catalysts, including rapid recombination of

photogenerated electron–hole pairs, a limited number of surface-active sites, inadequate absorption of visible light ( $\lambda < 450 \text{ nm}$ ), and slow reaction kinetics, have hindered their overall photoactivity.<sup>4</sup> A plethora of strategies have been previously reported to address these challenges. For example, hetero-elements (metal or non-metal) or  $\pi$ -molecular doping can be applied to modulate the surface and bulk characteristics of PCN. Likewise,  $\pi$ -molecular doping of PCN with aromatic functional groups including phenyl,<sup>5</sup> pyridine,<sup>6</sup> pyrimidine,<sup>7</sup> pyrazine,<sup>8</sup> thiazole,<sup>9</sup> benzothiazole,<sup>10</sup> caffeine,<sup>11</sup> nucleotides (adenine, guanine, cytosine, uracil, and thymine),<sup>12</sup> and thiophene,<sup>13</sup> is known to tailor the photo response and enhance photoactivity. This approach enables tuning of electronic energy levels, exciton migration behaviour, and microstructure of PCN, ultimately enhancing its photocatalytic performance.<sup>6,14</sup>

Incorporating non-metals such as F, Cl, Br, or I through elemental doping is another effective way to influence the electronic band structure of the PCN framework by reconstructing the corresponding highest occupied molecular orbital (HOMO) and lowest unoccupied molecular orbital (LUMO).<sup>15</sup> For example, Wang *et al.* created an extended aromatic heterocycle *via* iodine doping, which generated impurity energy levels near the valence band (VB) edge, resulting in an enhanced optical response and hydrogen evolution activity.<sup>16</sup> Similarly,

<sup>a</sup>Materials and Catalysis Laboratory, Department of Chemistry, Visvesvaraya National Institute of Technology (VNIT), South Ambazari Road, Nagpur 440010, India. E-mail: ssumare1965@gmail.com; vidyasagar.devthade@gmail.com

<sup>b</sup>Department of Chemical Engineering, Indian Institute of Technology Kanpur, Kanpur-208016, India

<sup>c</sup>Department of Chemistry, Bar-Ilan University, Ramat Gan 5290002, Israel

<sup>d</sup>School of Energy Engineering, Kyungpook National University, Buk-gu, Daegu, 41566, Republic of Korea

<sup>e</sup>Institute of Physical Chemistry, Polish Academy of Sciences, Kasprzaka 44/52, 01-224 Warsaw, Poland

<sup>f</sup>Department of Physics, Chungnam National University, 99 Daehak-ro, Yuseong-gu, Daejeon 34134, Republic of Korea

<sup>g</sup>Department of Chemistry, Indian Institute of Technology Hyderabad, Kandi, Sangareddy, 502285, India

<sup>h</sup>Institute for Environmental and Climate Technology, Korea Institute of Energy Technology (KENTECH), Naju 58330, Korea

† Electronic supplementary information (ESI) available. See DOI: <https://doi.org/10.1039/d3ta04938h>





**Photocatalytic Cr(vi) reduction and the RhB degradation experiment.** The photocatalytic experiments were performed in a custom-built photoreactor under visible-light irradiation. The visible-light source used was compact fluorescent lamps of 450–500 W m<sup>-2</sup> average intensity. In a typical Cr(vi) reduction experiment, 20 mg of catalyst was added to 100 mL of 10 mg L<sup>-1</sup> Cr(vi) solution. The source of Cr(vi) used in our study was potassium dichromate (K<sub>2</sub>Cr<sub>2</sub>O<sub>7</sub>). To act as a hole scavenger, 1 mM citric acid was added into the dispersion mixture. The mixture was then stirred in the dark for 30 min to achieve adsorption–desorption equilibrium. Subsequently, the mixture was irradiated with light while being continuously stirred, and sample aliquots were collected at a fixed period of illumination. The aliquots were then filtered by using a 0.45 μm syringe filter for further analysis. The reduction of Cr(vi) by the catalyst was evaluated using the 1,5-diphenylcarbazide (DPC) method as described in previous reports.<sup>21</sup> Initially, a 10 mM DPC solution was prepared in acetone. Then, 0.2 mL of DPC solution was added to 7 mL of 0.2 M H<sub>2</sub>SO<sub>4</sub> and thoroughly mixed. Afterward, 2 mL of the filtered aliquot was added to the mixture and kept undisturbed for 20 min to ensure complexation. The resulting magenta-coloured complex formed was then analysed by using a UV-vis spectrophotometer at a wavelength of 540 nm.

The RhB degradation experiments were performed in the same photoreactor setup. In a typical experiment, 100 mg of catalyst was dispersed in a 100 mL RhB (10 mg L<sup>-1</sup>) solution and stirred continuously for 30 min in the dark. The reaction mixture was then irradiated, and sample aliquots were collected at pre-decided time intervals. For analysis, the aliquot was collected and centrifuged to remove the residual catalyst. The resultant supernatants were then analysed using a UV-visible spectrophotometer at a wavelength of 554 nm.

**Computational details.** Density functional theory (DFT) calculations were performed under periodic boundary conditions using the generalized gradient approximation (GGA) of the Perdew–Burke–Ernzerhof (PBE) exchange correlation within the framework of the Vienna *ab initio* simulation package (VASP).<sup>23–25</sup> To describe the interactions between core and valence electrons, we employed the projector augmented wave (PAW) method.<sup>26</sup> The convergence criteria during structural optimization was set to 0.01 eV Å<sup>-1</sup> and 10<sup>-5</sup> eV for Hellman–Feynman atomic forces and the total energy threshold between two successive self-consistent electronic cycles, respectively. A kinetic energy cut-off of 500 eV and Monkhorst–Pack *k*-point grid of 7 × 7 × 1 are used for the plane wave expansion in the reciprocal space and to discretize the Brillouin-zone integration, respectively.<sup>27</sup> Grimme's D3 parametrization (DFT-D3) is employed to include the dispersion correction.<sup>28,29</sup> A vacuum of 15 Å is introduced along the *z*-direction to avoid artificial interactions between the adjacent units. Since band gaps are usually underestimated by standard DFT functionalization, the Heyd–Scuseria–Ernzerhof (HSE) formalism is used to perform hybrid DFT calculations with a 25% Hartree–Fock (HF) exchange.<sup>30–32</sup>

The adsorption energy between the surface and adsorbates ( $E_{\text{ads}}$ ) is computed using eqn (2).

$$E_{\text{ads}} = E_{\text{total}} - E_{\text{surface}} - E_{\text{adsorbate}} \quad (2)$$

where,  $E_{\text{total}}$ ,  $E_{\text{surface}}$  and  $E_{\text{adsorbate}}$  indicate the total energies of the adsorbed species on the surface, isolated surface, and adsorbates, respectively. Here, the energy of an isolated adsorbate molecule is computed in a cubic periodic box of 15 Å side length with a 1 × 1 × 1 Monkhorst–Pack *k*-point grid for Brillouin zone sampling, respectively. The zero-point energies (ZPE) and entropy (*S*) contributions are incorporated to compute the Gibbs free energy ( $\Delta G$ ) as shown below (eqn (3)).

$$\Delta G = \Delta E_{\text{H}} + \Delta E_{\text{ZPE}} - T\Delta S_{\text{H}} \quad (3)$$

where  $\Delta E_{\text{H}}$  is the DFT simulated reaction energy. *T* is the temperature (*T* = 298.15 K).  $\Delta S$  is the difference of vibration entropy between gas phase hydrogen and adsorbed hydrogen.  $\Delta E_{\text{ZPE}}$  is the zero-point energy corrections.

## Results and discussion

### Structure and optical features of 5-halouracil derived PCN

The thermal co-polymerization of PCN precursors with 5-halouracil yields the doping of  $\pi$ -aromatic uracil and halide ions (X: Cl<sup>-</sup>, Br<sup>-</sup>, and I<sup>-</sup>) into the core structure of PCN, as depicted in Fig. 1A.

The incorporation of the 5-halouracil moiety into the PCN framework induces structural modifications at the molecular level, thereby giving rise to altered physico-chemical properties. Hence, the investigation of alteration in the crystal structure of XUCN samples was conducted through powder X-ray diffraction (XRD) analysis. Pristine PCN has shown a low angle diffraction peak at 13.0°, which is due to the intraplanar stacking of the heptazine motif assigned to the (100) crystal plane (Fig. 1B). While peak at the higher angle, 27.7° corresponds to the heptazine motifs in melon stacked over one another. An analogous diffraction pattern was observed for the modified CUCN, BUCN, and IUCN samples. However, after the incorporation of 5-halouracil moieties, a notable decrease in the diffraction peak intensity was observed for XUCN samples. This indicates the distortion in the symmetrical planar structure of PCN. On comparing the relative intensity of diffraction peaks, CUCN exhibited the lowest peak intensity followed by BUCN and IUCN. This observation suggests that amongst all the 5-halouracils, the 5-chlorouracil (CU) moiety have the highest degree of interaction and influence on the crystalline architecture of the resultant PCN framework. This could be ascribed to the higher C–Cl bond strength and lower atomic radius of the chlorine atom. The larger atomic radius of bromine and iodine in comparison to chlorine hinders the probability of doping. In addition to the decreased diffraction intensity, the full width at half maxima ( $\beta$ ) corresponding to the (002) peak increased in the order PCN < IUCN < BUCN < CUCN. The broadening of ' $\beta$ ' indicates a decrease in the crystallite size. These findings affirm that the 5-halouracil moieties have a significant impact on PCN's crystal structure.

The XUCN samples further examined *via* Fourier transform-infrared spectroscopy (FTIR) revealed a distinctive out-of-plane





Fig. 1 Structure and optical properties. (A) Schematic illustration of the preparation of a 5-halouracil doped polymeric carbon nitride catalyst (XUCN), (B) powder X-ray diffraction (XRD) profiles, and (C) UV-visible diffuse reflectance spectra (UV-vis DRS) with digital photographs of powder catalyst as inset.

bending mode at  $810\text{ cm}^{-1}$ , which corresponds to the tri-s-triazine rings. (Fig. S1†), while the stretching modes of an aromatic C–N heterocycle were observed in the range of  $1000\text{--}1800\text{ cm}^{-1}$ . In addition, broad bands in the region of  $3000\text{--}3500\text{ cm}^{-1}$  were observed corresponding to the stretching vibration of terminal  $\text{--NH/–NH}_2$  and O–H bonds. The FTIR spectra indicate that the XUCN samples retain the basic carbon nitride structural features. Furthermore, a notable change in the intensity of bands was observed after incorporation of 5-halouracils. Specifically, the absorption bands at  $810$  and  $1000\text{--}1800\text{ cm}^{-1}$  that correspond to tri-s-triazine groups and the C–N heterocycle are much weaker for CUCN, showing altered heptazine structural connections. The FTIR result combined with XRD substantiates that the incorporation of 5-halouracil moieties into PCN rendered structural changes and disorder in the planar carbon nitride structure. To support the incorporation of a 5-halouracil moiety into the PCN backbone, solid-state cross polarized magic angle spinning (CP-MAS)  $^{13}\text{C}$  nuclear magnetic resonance (NMR) spectra of the PCN and BUCN catalyst were recorded. The  $^{13}\text{C}$  CP-MAS NMR spectrum of PCN shows two distinct signals at  $164.8$  and  $156.4$  ppm, that are assigned to the  $\text{sp}^2$  hybridized carbon atom in the  $\text{N–C=N}$

and  $\text{C–(N)}_3$  linkage of the heptazine core, respectively (Fig. S2A†).<sup>33</sup> In analogy with PCN, BUCN showcases similar characteristics signals to that of PCN with a slight shift. The shift in the major NMR signals could be due to the shielding effect of the electron withdrawing groups of the attached uracil moiety.<sup>34</sup> However, in addition to the representative signals corresponding to PCN, BUCN demonstrates additional signals affirming structural distortion and changes in the local carbon environment of BUCN due to the incorporation of 5-bromouracil moieties into the PCN backbone. The weak signals located at nearly  $167.1$ ,  $166.4$ , and  $159.5$  ppm are ascribed to the  $\text{C}_3$ ,  $\text{C}_4$ , and  $\text{C}_5$  carbon atoms in the BUCN structure as shown in Fig. S2B and C.† These findings show the successful incorporation of 5-bromouracil moieties into PCN. The elemental analysis of the samples further revealed no considerable change in the C : N : H values of XUCN catalysts in comparison to those of bulk PCN (Table S1†). The lack of measurable changes in elemental analysis of the catalyst composition could be due to insufficient doping concentration, stable catalyst structure, and surface vs. bulk level doping.

The ultraviolet-visible diffuse reflectance spectra (UV-vis DRS) of bulk PCN show an optical absorption edge at  $450\text{ nm}$ ,



which is due to the intrinsic  $\pi \rightarrow \pi^*$  electronic transition (Fig. 1C), caused by the  $\pi$ -conjugated aromatic framework and orderly packing of the heptazine tectonics in the polymeric structure.<sup>35</sup> On the other hand, the XUCN catalyst demonstrated extended visible light response (Fig. S3A†). By simply increasing the dopant concentration from 10 to 100 mg, the light absorption behaviour of XUCN samples shows a remarkable change (Fig. 1C). Importantly, as compared to bulk PCN, XUCN catalysts have significantly longer visible light absorption above 450 nm. The tailored optical response can be observed by the colour change from pale yellow to brownish yellow (inset of Fig. 1C). This is due to the newly emerged shoulder absorption peak between 450 and 800 nm, which is ascribed to the  $n \rightarrow \pi^*$  electronic transition involving lone pair electrons on edge nitrogen and halogen atoms.<sup>36</sup> This characteristic  $n \rightarrow \pi^*$  transition is spatially forbidden in PCN because of the perfectly symmetric and planar structural units. The appearance of  $n \rightarrow \pi^*$  transition is an indication of distortion in the planar and symmetric heptazine structure of XUCN catalysts. Furthermore, there is a noticeable change in visible-light absorption intensity corresponding to the  $n \rightarrow \pi^*$  electronic transition, with an increased intensity in the order IUCN < BUCN < CUCN. This observation implies that uracil moieties with halogen functionalities induce  $n \rightarrow \pi^*$  electronic transition and greatly expands the photo-response. CUCN exhibited the most prominent enhancement in the visible light response and  $n \rightarrow \pi^*$  electronic transition, which can be ascribed to the higher electronegativity and effective Cl-doping in the CUCN structure. The Tauc plot revealed a narrowed bandgap with the addition of 5-halouracil dopants (Fig. S3B†). Overall, pristine PCN has an estimated bandgap of 2.71 eV, whereas those of CUCN, BUCN, and IUCN are 2.57, 2.61, and 2.66 eV, respectively. Furthermore, it was observed that the CUCN and BUCN catalysts evinced the presence of mid-gap states, which were positioned above the valence band with transition energies of 1.81 and 1.88 eV, respectively (as depicted in the inset of Fig. S3B†). Conversely, neither PCN nor IUCN show the existence of mid-gap states due to their symmetrical planar structures and the absence of a shoulder peak, which can be attributed to the relatively low I-doping effect.<sup>37</sup> Theoretical explanation from a previous study suggests that doped halogen atoms contribute to the conduction band (CB) of the PCN electronic structure.<sup>19</sup> Due to the change in electronegativity of halogens, the configuration of CB experiences changes in the electronic band structure. Therefore, the reduced bandgap of XUCN catalysts is attributed to the different levels of doping and extended  $\pi$ -conjugated aromatic network.<sup>38</sup>

X-ray photoelectron spectroscopy (XPS) was applied to comprehend the chemical composition and bonding in PCN catalysts before and after 5-halouracil doping. The deconvoluted C 1s spectrum of PCN contained three peaks located at a binding energy value of 288.4, 285.5, and 284.8 eV, corresponding to the characteristic N-C=N linkage of the aromatic heptazine ring of PCN, C-NH<sub>x</sub> ( $x = 1, 2$ ) groups, and adventitious carbon (C-C/C=C), respectively (Fig. 2A).<sup>39</sup> On the other hand, four peaks were deconvoluted for all XUCN catalysts, of which three are consistent with those of PCN. The additional

featured peak at 287.9 eV is assigned to the signature C=O groups of the doped 5-halouracil moieties.<sup>40</sup> Compared to PCN, a noticeable increase in the peak area at 284.8 eV was also observed, which is an indication of increased adventitious carbon contribution. This is mainly because of the C-C/C=C bonds of 5-halouracil moieties attached to the heptazine core of PCN. The high-resolution N 1s XPS spectra of PCN and XUCN catalysts were fitted with identical peaks indicating that the nitrogen environment remains unaffected by the doping of 5-halouracils (Fig. S4†).<sup>41</sup> The O 1s spectrum of PCN demonstrated two peaks located at 533.4 and 531.8 eV ascribed to the surface adsorbed water and oxygen molecules, respectively (Fig. 2B).<sup>42</sup> Apart from the signature peaks, a third new peak appeared for the XUCN catalyst, which is assigned to the C=O group confirming the incorporation of the 5-halouracil moiety. To confirm the existence of halogen functionalities in the doped structure, the high-resolution spectrum of the corresponding doped halogen atom was obtained (Fig. 2C). The high-resolution Br 3d spectra of the BUCN catalyst is deconvoluted into three peaks located at 70.9, 68.4, and 66.9 eV. The two peaks at 70.9 and 68.4 eV can be assigned to the C-Br 3d<sub>3/2</sub> and C-Br 3d<sub>5/2</sub> covalent bonds, respectively,<sup>43,44</sup> while the third peak at 66.9 eV is likely from the ionic C-Br<sup>+</sup> 3d<sub>5/2</sub> bond.<sup>45</sup> The existence of ionic or semi-ionic bonds contributes significantly to improving the catalytic activity. This is due to the fact that these bonds serve as either electron acceptors or donors inducing the polarization of a  $\pi$ -electron cloud on polymeric network for effective charge transfer between halogen and carbon atoms.<sup>46</sup> This leads to higher conductivity as well as modified electronic properties. Furthermore, the Cl 2p XPS spectrum of CUCN is fitted with three peaks at 205.2, 201.3, and 196.9 eV allocated to the C-Cl 2p<sub>1/2</sub>, C-Cl 2p<sub>3/2</sub>, and C-Cl<sup>+</sup> 2p<sub>3/2</sub> bonds, respectively.<sup>48</sup> These findings indicate successful retention of bromine and chlorine in the BUCN and CUCN structures, respectively. Contrastingly, no peaks corresponding to iodine were detected in high resolution I 3d spectra of IUCN which is attributed to the cleavage of the fragile I-C bond during annealing and instability of the I-C type network.<sup>47</sup> Overall, XPS results confirm that the incorporation of 5-halouracil moieties into the triazine network stabilizes the bonding structures based on bromine and chlorine.

### Comprehensive analysis of morphology, microstructure, and electronic properties

The distinct variations in morphology and microstructure of modified XUCN were examined by field emission scanning electron microscopy (FE-SEM) and transmission electron microscopy (TEM). PCN exhibited 2D bulk sheet-like morphology with hardly any pores on the surface (Fig. S5 and S6†). In contrast, CUBU, BUCN, and IUCN catalysts demonstrated a porous broken-layered structure (Fig. 3A). It can be observed that CUCN shows a relatively higher order of porosity in comparison to BUCN and IUCN. Here, the high porosity of CUCN can be attributed to a higher degree of interaction of chlorine compared to bromine and iodine due to high electronegativity, small atomic size, and possible



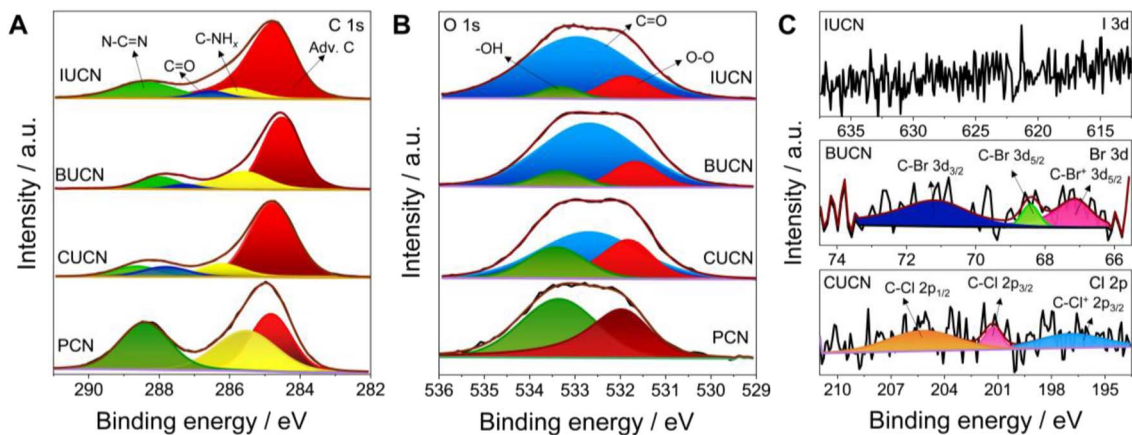


Fig. 2 Deconvoluted high-resolution X-ray photoelectron spectrum for (A) C 1s, (B) O 1s, and (C) Cl 2p, Br 3d, and I 3d of PCN and XUCN (X = Cl, Br, or I) samples.

vaporization of chlorine gas. Later, energy dispersive spectroscopy (EDS) employed to map the constituent elements revealed the uniformly dispersed C, N, O, and the

corresponding halogen elements (Cl, Br, and I on CUCN, BUCN, and IUCN, respectively) on the surface of the XUCN matrix (Fig. S7–S9<sup>†</sup>). Furthermore, the constituent weight

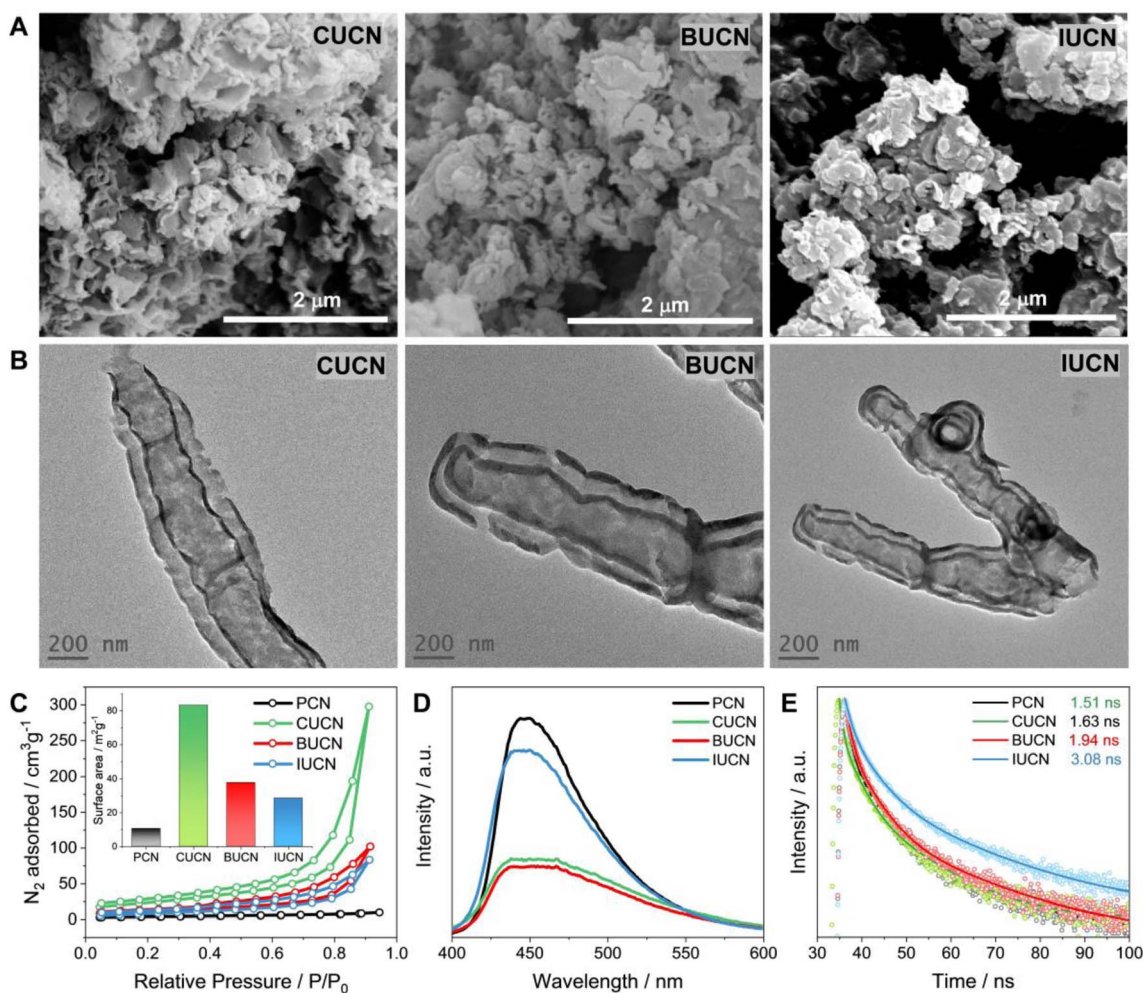


Fig. 3 Morphology and optical properties. (A) Field emission scanning electron microscopy (FE-SEM) images (B) transmission electron microscopy (TEM) images, (C) nitrogen adsorption–desorption isotherm (the calculated surface area values are in the inset), (D) room temperature photoluminescence (PL) spectra, and (E) time-resolved photoluminescence (TR-PL) spectra of PCN, and XUCN (X = Cl, Br, or I) samples.



percentage was estimated by using EDX spectra. The EDX spectra of CUCN and BUCN revealed the presence of 0.2 and 0.1 wt% of chlorine and bromine, respectively (Fig. S7 and S8†). However, due to low doping probability, iodine could not be detected in the EDX spectrum of IUCN (Fig. S9†). The porous layered structure of XUCN catalysts was further visualized by using the TEM images. However, the high-resolution TEM (HR-TEM) images of all the materials demonstrated a hollow tubular type microstructure feature at the edge (Fig. 3B). The observed phenomenon can be attributed to the alteration of the molecular van der Waals force resulting from the inclusion of halouracil, which facilitates the bending and flexibility of the edges. The results support the substantial impact of 5-halouracil moieties on the morphological and microstructural characteristics of the modified PCN. The porous nature of the XUCN materials is further confirmed by using the nitrogen adsorption-desorption isotherm, which indicates a micro/mesoporous structure with slit-shaped pores as evidenced by a Type IV isotherm and typical H3 hysteresis loop.<sup>48</sup> The measured surface property parameters are presented in Table S2.† The specific surface area ( $S_{\text{BET}}$ ) values of XUCN samples are higher as compared to those of their PCN counterparts and follow the order PCN < IUCN < BUCN < CUCN (inset of Fig. 3C, Table 1). The highest surface area of CUCN can be attributed to the higher degree of interaction between reactant molecules and smaller atomic radius of Cl. Moreover, the pore radius ( $D_r$ ) and pore volume ( $D_v$ ) values of XUCN samples exhibit a significant increase compared to those of PCN. Hence, XUCN samples provide large active surface area to reactant molecules by exposing more surface-active sites. Next, the effect of halogen doping on the dissociation and migration of photo-excitons was systematically investigated using room temperature photoluminescence (PL) and time-resolved photoluminescence (TR-PL) spectroscopy. A significant quenching in PL intensity is observed after 5-halouracil doping in PCN, indicating that the doping enhances the separation of photogenerated charge carriers (Fig. 3D). The TR-PL spectra of PCN and XUCN catalysts exhibit triexponential decay, indicative of multiple relaxation (Fig. 3E, Table S3†). The estimated average lifetime ( $\tau_{\text{avg}}$ ) of PCN, CUCN, BUCN, and IUCN is found to be 1.51, 1.63, 1.94, and 3.08 ns, respectively (Table 1). The increased lifetime for the XUCN catalysts indicates enhanced possibility of photoexcitons to participate in the photocatalytic reaction before recombination.<sup>4</sup> Further

to be noted that the  $\tau_{\text{avg}}$  of XUCN catalysts decreases with decreasing halogen atom size, highlighting the influence of the halogen atom on the electron lifetime decay.

The paramagnetic properties of PCN and XUCN were probed through room temperature electron paramagnetic resonance (EPR) spectroscopy. PCN exhibited a Lorentzian line with a Lande  $g$ -factor of 2.0036 (Fig. S10†) indicating delocalized unpaired electrons that are generated on the  $sp^2$ -carbon atom of the  $\pi$ -conjugated aromatic rings.<sup>49</sup> In contrast, the XUCN catalysts showed a Lorentzian line which shifted to a lower  $g$ -value of 1.9873. This shift in the  $g$ -value provides crucial information regarding the intrinsic properties of the paramagnetic centre, chemical structure (localized or delocalized structure), and spin states.<sup>50</sup> The high and low  $g$ -values represent a delocalized and localized  $\pi$ -conjugated structure, respectively. The downshifted  $g$ -value EPR signals of CUCN, BUCN, and IUCN, indicate the formation of a localized  $\pi$ -conjugated structure. Furthermore, compared to PCN, XUCN catalysts demonstrated intensified Lorentzian lines in the order PCN < IUCN < CUCN < BUCN. This increase in intensity implies the enhanced generation of unpaired electrons over the XUCN catalyst, with BUCN showing superiority in producing unpaired electrons over the others. Overall, the EPR results exemplify that 5-halouracil doping in PCN results in the formation of localized  $\pi$ -conjugated structures that generate more unpaired electrons.

### Boosting PCN photocatalytic activity through 5-halouracil doping

**Photocatalytic  $\text{H}_2\text{O}_2$  generation and  $\text{H}_2$  evolution activity of 5-halouracil derived PCN photocatalysts.** The photoactivity of the synthesized PCN and XUCN catalysts was initially assessed for the photocatalytic oxygen reduction reaction (ORR) to generate  $\text{H}_2\text{O}_2$ , using 10% IPA solution as a sacrificial reagent under a saturated  $\text{O}_2$  atmosphere. Following 4 h of light exposure, the PCN photocatalyst produced a mere 193.2  $\mu\text{M}$  of  $\text{H}_2\text{O}_2$ . In contrast, the XUCN catalysts doped with 5-halouracil exhibited a relatively high  $\text{H}_2\text{O}_2$  production, which is attributed to their modified physicochemical properties (Fig. 4A). Among all the XUCN catalysts, the BUCN catalyst demonstrated the highest  $\text{H}_2\text{O}_2$  yield of 506.18  $\mu\text{M}$ , which is twice that of the unmodified PCN. Additionally, the photocatalytic rate of  $\text{H}_2\text{O}_2$  formation reached 126.6  $\mu\text{mol h}^{-1}$ , significantly surpassing that of PCN (48.3  $\mu\text{mol h}^{-1}$ ), CUCN (66.7  $\mu\text{mol h}^{-1}$ ), and IUCN (97.2  $\mu\text{mol h}^{-1}$ ) and is competitive to several state-of-the-art PCN-based photocatalysts (Fig. 4B and C, Table S4†). The underlying reasons for the enhanced performance of the BUCN catalyst compared to that of PCN as well as CUCN and IUCN is discussed in the later section. Furthermore, the  $\text{H}_2\text{O}_2$  formation activity of the BUCN catalyst was evaluated through repetitive cycles to assess its cyclic  $\text{H}_2\text{O}_2$  generation capability and structural stability. The cyclic experiments demonstrated that BUCN maintains a high  $\text{H}_2\text{O}_2$  yield for five consecutive cycles (Fig. S11†). Moreover, the XRD pattern and FTIR spectrum of the recycled BUCN catalyst showed no discernible changes after the fifth cycle (Fig. S12a and b†). Furthermore, the UV-DRS spectrum of the BUCN catalysts has shown a similar optical

Table 1 Physicochemical parameters of PCN and XUCN catalysts

Catalysts	$E_g^a$ (eV)	$S_{\text{BET}}^b$ ( $\text{m}^2 \text{g}^{-1}$ )	$D_v^c$ ( $\text{cm}^3 \text{g}^{-1}$ )	$D_r^d$ (nm)	$\tau_{\text{avg}}^e$ (ns)
PCN	2.71	11	0.013	1.23	1.5
CUCN	2.57	83	0.155	1.63	1.6
BUCN	2.61	38	0.084	1.64	1.9
IUCN	2.66	29	0.061	1.62	3.1

<sup>a</sup> Bandgap estimated from UV-DRS measurements. <sup>b</sup> BET specific surface area calculated from the  $\text{N}_2$  adsorption-desorption isotherm. <sup>c</sup> BJH pore volume. <sup>d</sup> BJH pore radius. <sup>e</sup> Average lifetime of photoexcitation.





Fig. 4 Photocatalytic performance. (A) photocatalytic H<sub>2</sub>O<sub>2</sub> production as a function of irradiation time under visible light ( $\lambda > 450$  nm) with 10 vol% isopropanol, (B) rate of H<sub>2</sub>O<sub>2</sub> generation over PCN and XUCN catalysts, (C) a comparison of the H<sub>2</sub>O<sub>2</sub> rate production with state-of-art PCN-based catalysts; more details can be found in the Table S4, ESI† (D) photocatalytic H<sub>2</sub> production and the corresponding (E) H<sub>2</sub> production rate constants over PCN and XUCN catalysts.

response, and the bandgap was also found to be intact indicating no significant deactivation of the BUCN catalyst during a continuous 20 h measurement period.

The photocatalytic H<sub>2</sub> evolution ability of PCN and XUCN catalysts was evaluated under visible light irradiation ( $\lambda > 420$  nm), employing 1 wt% Pt as a co-catalyst and 10% TEOA as a sacrificial donor. Like the high H<sub>2</sub>O<sub>2</sub> production activity, the XUCN catalysts showcased a significant enhancement in the photocatalytic H<sub>2</sub> generation activity compared to PCN after a reaction time of 4 h (Fig. 4D). Notably, the BUCN catalyst displayed the highest H<sub>2</sub> production rate of 0.563 mmol g<sup>-1</sup> h<sup>-1</sup>, nearly three times that of PCN (0.260 mmol g<sup>-1</sup> h<sup>-1</sup>) (Fig. 4E). Furthermore, the apparent quantum yield (AQY) for H<sub>2</sub>

generation was calculated to be 2.62% for the BUCN catalyst at 420 nm. All the XUCN catalysts outperformed the hydrogen generation capabilities of a bare PCN catalyst. The optical, textural, and dynamic studies suggest that the increased photocatalytic activity of the XUCN catalysts compared to PCN can be ascribed to their broad optical response, and relatively higher specific surface area due to their porous structure. Additionally, the intimate interaction between the doped uracil and halide ions extends the  $\pi$ -conjugated system, thereby facilitating the mobility of photo-excited electrons. To note, the BUCN catalyst exhibited the highest PL quenching ability compared to the CUCN and IUCN catalysts. Despite the higher surface area exhibited by CUCN, BUCN demonstrated a higher





photocatalytic  $\text{H}_2\text{O}_2$  yield. This discrepancy is likely due to the valence electrons of Br-atoms being less electronegative than those of Cl-atoms, resulting in greater delocalization and interaction with the  $\pi$ -electron cloud of PCN. Conversely, doped I-atoms, despite possessing less electronegativity than Br-atoms, fail to interact with the  $\pi$ -electron cloud of PCN due to their large atomic radius, resulting in a lower doping probability. These factors collectively contribute to the enhanced photocatalytic activity of the BUCN catalyst. The findings underscore the important role of halogen ions in the photocatalytic ORR activity for  $\text{H}_2\text{O}_2$  production and hydrogen generation.

**Photocatalytic hexavalent chromium reduction and rhodamine B degradation activity.** The as-prepared catalysts were further employed as photocatalysts for aqueous phase reduction of hexavalent chromium ( $\text{Cr}(\text{VI})$ ) and the degradation of a model pollutant rhodamine B (Rh B) dye. The  $\text{Cr}(\text{VI})$  reduction experiments were conducted under visible light irradiation, with citric acid (0.1 mmol) serving as the hole scavenger, and the results were evaluated using the 1,5-diphenylcarbazide (DPC) method.<sup>21</sup> The  $\text{Cr}(\text{VI})$  reduction efficiency was analysed as a function of irradiation time (Fig. 5A), and pristine PCN displayed 40% reduction efficiency in 50 min of light irradiation. In comparison, the CUCN, BUCN, and IUCN catalysts exhibited enhanced reduction within the same timeframe (Fig. 5A), with a significant increase in the rate of reduction (0.047, 0.068, and 0.061  $\text{min}^{-1}$  for CUCN, BUCN, and IUCN, respectively) as compared to that of PCN (0.008  $\text{min}^{-1}$ ) (Fig. S13†). A steady

decay in absorption maxima at 540 nm shows a rapid  $\text{Cr}(\text{VI})$  reduction phenomenon (Fig. S14†). The underlying reason for this outcome is discussed in the previous section. Furthermore, a set of control experiments carried out under dark conditions and without a catalyst, revealed no significant  $\text{Cr}(\text{VI})$  reduction. This implies that the reduction reaction was the result of the synergistic effect of the catalyst and light irradiation. Moreover, quantitative  $\text{Cr}(\text{VI})$  reduction was evaluated by increasing the concentration of  $\text{Cr}(\text{VI})$  (10, 20, 30, 40, and 50  $\text{mg L}^{-1}$ ) while maintaining a constant catalyst dose (0.5  $\text{g L}^{-1}$ ), and the corresponding reduction rate was assessed for the BUCN catalyst (Fig. S15†). With an increase in the concentration, BUCN required more time to achieve complete reduction of  $\text{Cr}(\text{VI})$ , and as a result, the rate constant calculated by the pseudo-first-order kinetic fit decreased as the  $\text{Cr}(\text{VI})$  concentration increased. This exemplifies that high concentration of  $\text{Cr}(\text{VI})$  can be reduced over the BUCN catalyst by merely prolonging the irradiation time. In addition to  $\text{Cr}(\text{VI})$  concentration, impact of the catalyst dosage was evaluated by varying the amount of catalyst. Reducing the dosage from 0.5 to 0.1  $\text{g L}^{-1}$  resulted in a severe drop in the reduction efficiency, whereas increasing the dosage to 2  $\text{g L}^{-1}$  led to a reduction efficiency of 96% in just 30 min of irradiation (Fig. S16†). Meanwhile, with a moderate amount of catalyst (0.5  $\text{g L}^{-1}$ ), BUCN exhibited recyclability up to five cyclic  $\text{Cr}(\text{VI})$  reductions with 91% efficiency at 10  $\text{mg L}^{-1}$   $\text{Cr}(\text{VI})$  concentration (Fig. 5B). To further evaluate the impact of pH on the  $\text{Cr}(\text{VI})$  reduction performance of the BUCN catalyst, we conducted experiments with pH values ranging from 2 to 10

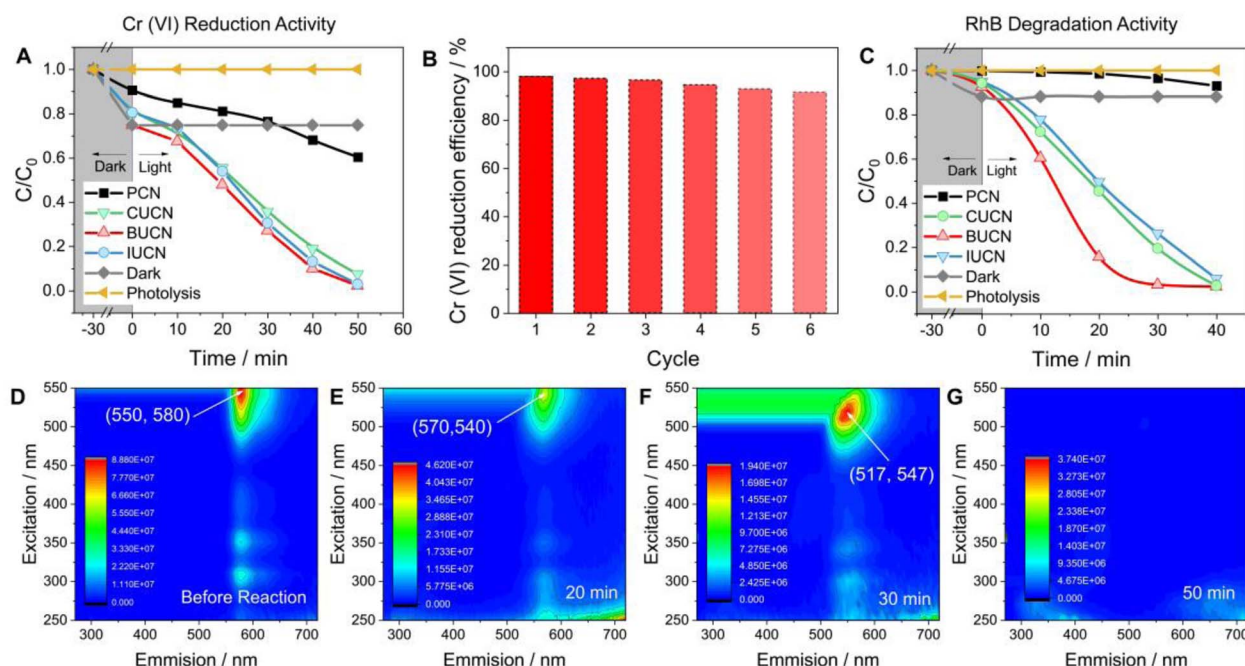


Fig. 5 Photocatalytic removal of aquatic pollutants: (A) photocatalytic  $\text{Cr}(\text{VI})$  reduction performance of PCN and UCN catalysts (reaction conditions: 20 mg of catalyst, 100 mL  $\text{Cr}(\text{VI})$  solution of 10  $\text{mg L}^{-1}$ ), (B) cyclic durability test of an optimized BUCN catalyst for  $\text{Cr}(\text{VI})$  reduction during repetitive six cycles, (C) relative decrease in rhodamine B (RhB) concentration as a function of time over PCN and UCN photocatalysts under visible light irradiation, and the corresponding 3D excitation-emission (3D EEM) matrix of (D) untreated RhB stock solution (before reaction), and photocatalytically treated RhB solution with a BUCN catalyst after (E) 20 min, (F) 30 min, and (G) 50 min of visible light irradiation, respectively.



(Fig. S17†). The results showed that as the pH decreases, the Cr(VI) reduction activity increases significantly, with the highest 99.2% reduction at pH = 2 in 50 min of light irradiation. The presence of Cr(VI) in the form of dichromate ( $\text{Cr}_2\text{O}_7^{2-}$ ) and hydrogen dichromate ( $\text{HCrO}_4^-$ ) facilitates their electrostatic interaction with the catalyst surface in acidic pH, while the presence of  $\text{OH}^-$  under alkaline conditions induces electrostatic repulsion between the existing chromium ions and catalyst's surface inhibiting the reduction reaction.<sup>51</sup>

The XUCN photocatalyst demonstrated a higher rate of photooxidative degradation of rhodamine B (RhB, 20 mg L<sup>-1</sup>) compared to the bare PCN counterpart (Fig. 5C). BUCN exhibited the highest degradation rate constant of 0.116 min<sup>-1</sup> (0.002 min<sup>-1</sup> for PCN) (Fig. S18†). Furthermore, the control experiments suggested a completely photooxidative RhB degradation process on the catalyst's surface. To investigate the photocatalytic degradation process and dissolved organic matter in residual RhB solution after illumination, 3D excitation emission matrix (3D-EEM) fluorescence spectroscopy was used (Fig. 5D–G). The 3D-EEM of untreated RhB solution (stock) revealed a characteristic fluorescence peak centred at an excitation/emission value of 550/580 nm.<sup>52</sup> As the photocatalytic reaction progressed, the intensity of the peak decreased significantly after 20 min, indicating the predominant decolouration process of RhB and generation of photo-transformation intermediates.<sup>53</sup> After 30 min of irradiation, the peak was blue shifted to 517/547 nm, which was attributed to the dissociation of large organic molecules into smaller fragments, cleavage of RhB's chromophoric structure, and elimination of functional groups.<sup>54</sup> This observation suggests the *N*-deethylation process of RhB molecules and fragmentation of *N*-deethylated intermediates into small molecules. Interestingly, the peak disappeared after 50 min of irradiation, indicating the complete decomposition of RhB molecules and their mineralization into  $\text{CO}_2$  and  $\text{H}_2\text{O}$ .<sup>55</sup>

Overall, the photocatalytic experiments reveal a higher photocatalytic activity for the prepared BUCN catalyst compared to the PCN and other XUCN catalysts (Table 2). The excellent photoactivity of the BUCN catalyst can be ascribed to its physicochemical properties as discussed in the previous section.

**Molecular and binding energies analysis of 5-halouracil doped PCN.** To gain deep insights into the 5-halouracil doping effect on the photocatalytic oxygen reduction reaction (ORR) activity, we performed density functional theory (DFT) calculations on various 5-halouracil doped structures (Fig. 6A). Aiming

to assess the stability of doped structures, we computed the adsorption energies ( $E_{\text{ads}}$ ) of 5-halouracil molecules embedded in the PCN framework. The negative binding energies of -0.32, -0.33, and -0.35 eV for CUCN, BUCN, and IUCN, respectively, indicate the thermodynamic stability and easier synthesis. Furthermore, the C–N bond length close to the uracil molecule was significantly increased compared with that of PCN structure indicating a certain degree of structural deformation after doping. Furthermore, the difference in the carbon-halogen bond lengths can be ascribed to the difference in electronegativity and radius of the respective atoms (Table 3). Typically, the ORR activity for  $\text{H}_2\text{O}_2$  production is highly dependent on the formation and desorption of  $^*\text{OOH}$ , where the maximum activity for an ideal catalyst can be obtained at an optimized binding (neither too strong nor too weak) of a  $^*\text{OOH}$  intermediate. Hence, the  $^*\text{OOH}$  binding energies ( $\Delta G_{^*\text{OOH}}$ ) are generally treated as a universal indicator to estimate the catalytic performance. In addition to this, the  $\text{H}^+$  and  $\text{O}_2$  adsorption plays a crucial role in the formation of the  $^*\text{OOH}$  intermediate, and thus, we calculated the corresponding binding energies on pure and 5-halouracil doped PCN surfaces. The optimized structures of  $\text{H}^+$  and  $\text{O}_2$  adsorbed PCN and XUCN are shown in Fig. 6B and C. The  $\text{H}^+$  adsorption energies of XUCN obtained are found to be smaller than that of the pure PCN counterpart, indicating the importance of 5-halouracil in tuning the  $\text{H}^+$  adsorption for promoting the subsequent proton-coupled electron transfer step of  $^*\text{OOH}$  to  $\text{H}_2\text{O}_2$  (Table 3). The  $\text{O}_2$  adsorption energies of 5-halouracil doped PCN are also lower than that of PCN, indicating that the former efficiently activates  $\text{O}_2$  (Table 3). The comparison of the reaction free energy diagram for pure and 5-halouracil doped PCN is shown in Fig. 6D. For an ideal catalyst, the binding strength of  $\text{OOH}^*$  ( $\Delta G_{^*\text{OOH}}$ ) at 0.70 V vs. CHE is 3.52 eV at zero thermodynamic limiting potential.<sup>11,12</sup> Accordingly, a higher or lower  $\Delta G_{^*\text{OOH}}$  with respect to the ideal value indicates under binding or over binding of  $^*\text{OOH}$ , respectively. Clearly, the  $^*\text{OOH}$  formation over 5-halouracil doped PCN is towards the optimal value compared to pure PCN (Table 3). Specifically, the  $\text{HOO}^*$  binding energy of BUCN is slightly lower and closer to that of the ideal catalyst, suggesting the highest catalytic activity and selectivity towards  $\text{H}_2\text{O}_2$  generation. The strong interaction is further confirmed by the charged density difference, where there is a charge redistribution between 5-halouracil doped PCN and the  $^*\text{OOH}$  intermediate (Fig. 6E), indicating prominent  $\text{H}_2\text{O}_2$  generation. Furthermore, the density of state calculations demonstrates

Table 2 Comparison table of the photocatalytic activity of as-prepared PCN and XUCN catalysts

Catalyst	$\text{H}_2\text{O}_2$ production rate ( $\mu\text{mol h}^{-1}$ )	$\text{H}_2$ evolution rate ( $\text{mmol h}^{-1} \text{g}^{-1}$ )	Rate constant	
			Cr(VI) reduction	RhB degradation
PCN	48.3	0.260	0.008	0.002
CUCN	66.7	0.486	0.047	0.052
BUCN	126.6	0.563	0.068	0.116
IUCN	97.2	0.520	0.061	0.043



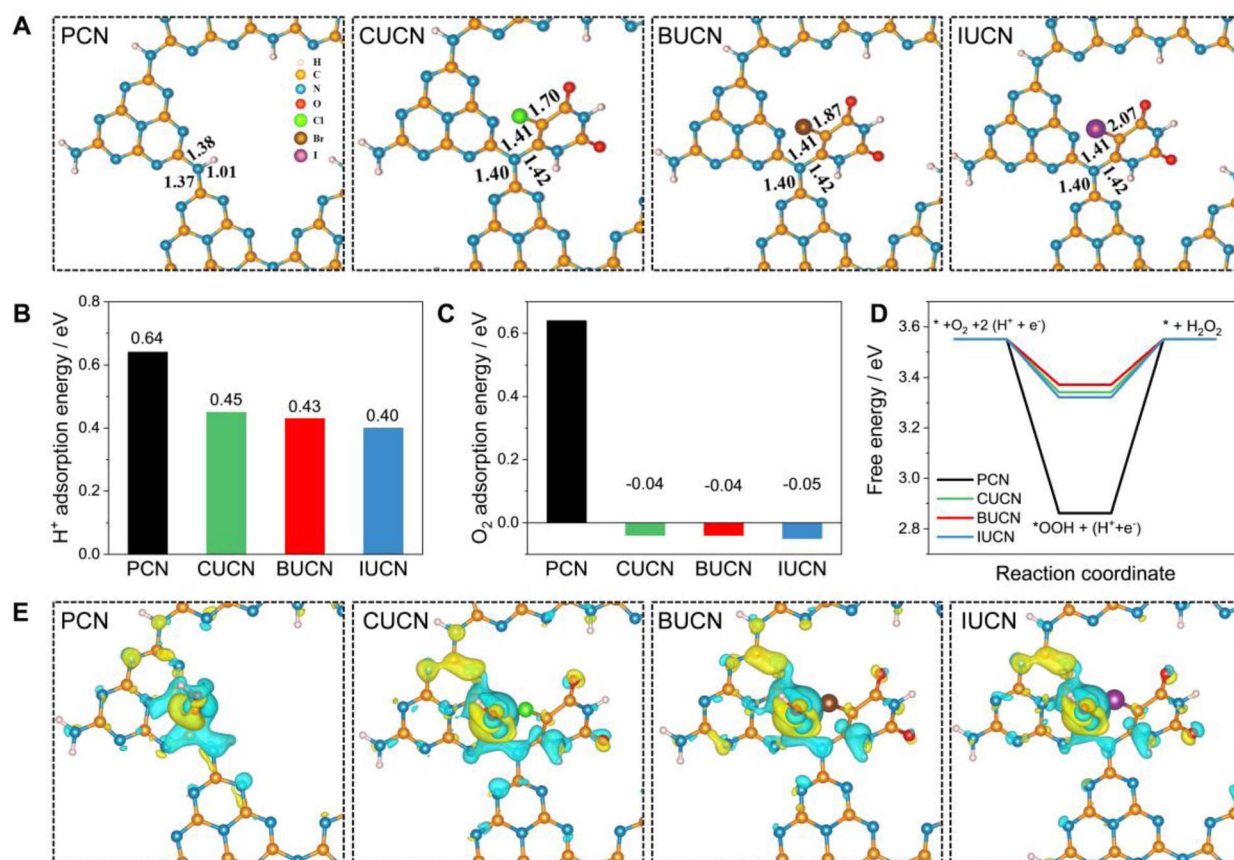


Fig. 6 Theoretical analysis: (A) optimized structures of PCN, and XUCN configurations, (B) proton ( $\text{H}^+$ ) adsorption and (C) oxygen ( $\text{O}_2$ ) adsorption energies on pristine PCN and halouracil doped PCN, and (D) free energy profile of photocatalytic  $\text{O}_2$  reduction to hydrogen peroxide ( $\text{H}_2\text{O}_2$ ) over PCN and XUCN catalysts at  $U = 0.7$  V, and (E) charge density difference of  $\text{OOH}^*$  species adsorbed on PCN and XUCN catalysts (the yellow and blue iso-surface represents electron accumulation and depletion regions, respectively).

that the band gap of PCN is reduced after the introduction of 5-bromouracil, where the valence band maximum (VBM) is dominated by 5-bromouracil and conduction band minimum (CBM) is constructed from PCN as shown in Fig. S18.† Thus, a new electron-transfer pathway is formed by the introduction of 5-bromouracil into PCN that connects the N-atoms, which enhances the photocatalytic efficiency by promoting carrier migration.

**Underlying photocatalytic mechanism.** To elaborate the ORR mechanism to generate  $\text{H}_2\text{O}_2$ , control experiments were conducted by varying the reaction atmosphere and using  $\text{AgNO}_3$  and *p*-benzoquinone (*p*-BQ) as electron and superoxide radical ( $\text{O}_2^-$ ) scavengers, respectively. When the experiment was

conducted under an open atmosphere, the  $\text{H}_2\text{O}_2$  yield lowered significantly, which is an indication that saturated  $\text{O}_2$  atmospheric conditions are required to achieve higher  $\text{H}_2\text{O}_2$  yield (Fig. S20†). This observation was further supported by the control experiment in an exclusive  $\text{N}_2$  atmosphere, where no  $\text{H}_2\text{O}_2$  was detected. Furthermore, the  $\text{H}_2\text{O}_2$  yield severely dropped on adding  $\text{AgNO}_3$  and *p*-BQ, suggesting that  $\text{H}_2\text{O}_2$  formation occurs *via* reduction of  $\text{O}_2$  by photogenerated electrons, and  $\text{O}_2^-$  functions as a crucial intermediate for  $\text{H}_2\text{O}_2$  generation. Additionally, RhB degradation was also assessed using sacrificial agents, isopropanol (IPA, as an  $\text{OH}^-$  scavenger), ammonium oxalate (AO, as an  $\text{h}^+$  scavenger), and *p*-BQ. It was observed that the RhB degradation performance of the BUCN

Table 3 Density functional theory derived parameters for the optimized PCN and XUCN structures

Sample	C-N bond length (Å)	C-X bond length (Å)	$\text{H}^+$ adsorption energy (eV)	$\text{O}_2$ adsorption energy (eV)	$\Delta G_{\text{OOH}^*}$ (eV)
PCN	1.37	—	0.64	0.64	2.86
CUCN	1.40	1.70	0.45	-0.04	3.34
BUCN	1.40	1.87	0.43	-0.04	3.37
IUCN	1.40	2.07	0.40	-0.05	3.32



catalyst severely dropped to 32% on employing *p*-BQ, signifying that the  $\cdot\text{O}_2^-$  plays a crucial role in RhB degradation performance (Fig. S21†).

The electron spin resonance (ESR) spin trapping experiment was performed to gain further insights into the generation of reactive oxidative species (ROS),  $\cdot\text{O}_2^-$  and  $\cdot\text{OH}$ . Under light irradiation the ESR spectra of PCN and XUCN catalysts exhibited characteristic four-line signals using 5,5-dimethyl-1-pyrroline N-oxide (DMPO) with a peak intensity ratio of 1 : 2 : 2 : 1, indicating the generation of  $\cdot\text{OH}$  radicals on PCN and XUCN (Fig. S22A†). Remarkably, the XUCN catalysts showed heightened signal intensity with respect to PCN. Later, the spin trapping experiment by adding DMSO along with DMPO effectively split the ESR signal into radical adducts indicating the generation of  $\cdot\text{O}_2^-$ . This finding indicates that XUCN catalysts are more capable in the generation of  $\cdot\text{O}_2^-$  than bulk PCN (Fig. S22B†).

The presence of bromide ions ( $\text{Br}^-$ ) in XUCN catalysts has a significant impact on the photocatalytic mechanism. The  $\text{Br}^-$  acts as electron acceptors and enhance the generation of ROS, such as  $\cdot\text{OH}$  radicals and  $\cdot\text{O}_2^-$ , leading to improved photocatalytic performance. This is supported by the heightened signal intensity observed in the ESR spectra of XUCN catalysts compared to those of PCN, indicating increased generation of  $\cdot\text{OH}$  radicals and  $\cdot\text{O}_2^-$ . Thus, the presence of  $\text{Br}^-$  ions contributes to the overall efficiency of the photocatalytic process and enhances the degradation performance of the catalyst.

Based on the experimental and theoretical calculations, a plausible mechanism on the BUCN catalyst is depicted in Scheme 1. Under light irradiation, BUCN absorbs photons and generates electron-hole pairs. The reconstructed electronic energy levels cause the electron-hole couples to dissociate rapidly. On the other hand, the high surface area and low adsorption energy enable better adsorption of  $\text{H}^+$  and  $\text{O}_2$  on the BUCN surface. The synergy between photo-exciton dissociation

and efficient adsorption behaviour promotes  $2e^- \text{O}_2$  reduction to generate  $\text{H}_2\text{O}_2$ . The  $\text{O}_2$  can accept one electron to generate  $\cdot\text{O}_2^-$  and then  $\cdot\text{O}_2^-$  takes another electron to generate  $\text{H}_2\text{O}_2$ . According to this observation and in conjunction with previous reports, photogenerated electrons reduce  $\text{O}_2$  to generate  $\text{H}_2\text{O}_2$  (eqn (4)).



Consequently, the dissociated electrons accelerate the water reduction reaction producing hydrogen. These electrons are also responsible for the reduction of the  $\text{Cr}(\text{vi})$  species. However, in the case of RhB degradation, photogenerated electrons react with dissolved oxygen to produce  $\cdot\text{O}_2^-$ . These  $\cdot\text{O}_2^-$  oxidise RhB molecules, mineralizing them into innocuous products.

## Conclusion

In summary, 5-halouracil derivatives were used to incorporate both a  $\pi$ -conjugated organic moiety and halogen atoms into the PCN framework. 5-halouracil doped PCN (XUCN, X = Cl, Br, or I) exhibited a significantly extended visible-light response above 450 nm, tailored the surface topological features, and accelerated the exciton dissociation. The photoactivity assessment revealed that the BUCN catalyst exhibits  $\text{H}_2\text{O}_2$  and hydrogen generation rate of  $126.6 \mu\text{mol h}^{-1}$  and  $0.563 \text{ mmol g}^{-1} \text{ h}^{-1}$ , which is much higher than that of pristine PCN. In addition, BUCN exhibited over 95%  $\text{Cr}(\text{vi})$  reduction activity in 50 min of irradiation and achieved complete mineralization of RhB dye into  $\text{CO}_2$  and  $\text{H}_2\text{O}$  in 50 min of visible light irradiation. Furthermore, theoretical investigation unveiled the low  $\text{H}^+$  and  $\text{O}_2$  adsorption energy for BUCN that accelerated the  $\text{H}_2\text{O}_2$  and hydrogen generation performance. The experimental results in conjunction with theoretical calculations clarify the boosted photocatalytic activity of the BUCN catalyst. We believe the results provided here will motivate the use of the one-step dual doping approach to systematically tweak the optoelectronic characteristics of PCN and accomplish superior photocatalytic performance for both energy and environmental applications.

## Author contributions

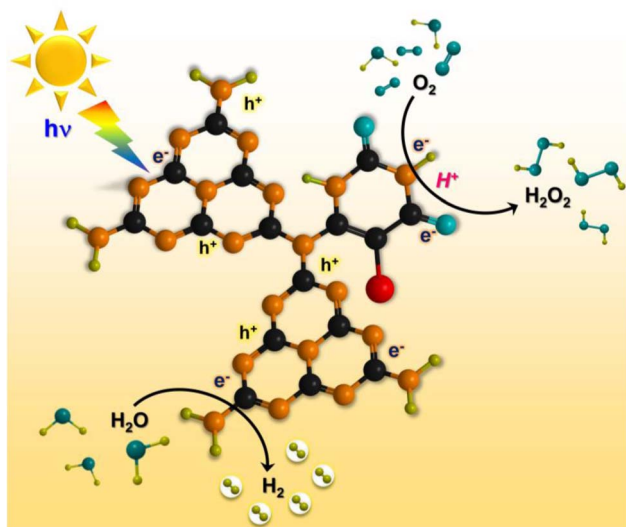
T. B. and V. D. conceptualized the project. T. B. developed experimental design and methodology. S. S. U. supervised the project. T. B., B. M. A., A. G., D. J. K., N. M., D. V., and S. S. U. investigated and formally analysed the results. T. B. wrote the original draft and B. M. A., A. G., D. J. K., N. M., K. S. P., D. V., and S. S. U. revised and edited the manuscript.

## Conflicts of interest

There are no conflicts to declare.

## Acknowledgements

TB would like to thank the Director, VNIT, Nagpur, for the doctoral fellowship. We would like to thank the Department of



Scheme 1 Schematic illustration of photocatalytic  $\text{H}_2\text{O}_2$  production and hydrogen generation (the black, orange, blue, green, and red spheres represent C, N, O, H, and halogen ions).



Science and Technology Fund for Improvement of Science and Technology Infrastructure (DST-FIST) through project no. SR/FST/CSI-279/2016(C) for providing the instrumentation facility at the Department of Chemistry, VNIT, Nagpur. We thank SAIF IIT Madras and IIT Bombay for the central instrumentation facility. BMA would like to thank the HPC centre, IIT Kanpur for providing the computational facilities. NRM is thankful to PASIFIC postdoctoral funding received from the European Union's Horizon 2020 research and innovation program under the Marie Skłodowska-Curie grant agreement No. 847639 and from the Ministry of Education and Science.

## Notes and references

- 1 Y. Wang, S. Z. F. Phua, G. Dong, X. Liu, B. He, Q. Zhai, Y. Li, C. Zheng, H. Quan and Z. Li, *Chem*, 2019, **5**, 2775–2813.
- 2 X. Wang, K. Maeda, A. Thomas, K. Takanebe, G. Xin, J. M. Carlsson, K. Domen and M. Antonietti, *Nat. Mater.*, 2009, **8**, 76–80.
- 3 D. Vidyasagar, T. Bhojar, G. Singh and A. Vinu, *Macromol. Rapid Commun.*, 2021, **42**, 2000676.
- 4 Q. Zhou, Y. Guo, Z. Ye, Y. Fu, Y. Guo and Y. Zhu, *Mater. Today*, 2022, **58**, 100–109.
- 5 Y. Wang, K. Wang, F. Dai, K. Zhang, H. Tang, L. Wang and J. Xing, *Nat. Commun.*, 2022, **13**, 6495.
- 6 T. Bhojar, D. J. Kim, B. M. Abraham, S. Tonda, N. R. Manwar, D. Vidyasagar and S. S. Umare, *Appl. Catal., B*, 2022, **310**, 121347.
- 7 L. Heymann, S. C. Bittinger and C. Klinke, *ACS Omega*, 2018, **3**, 17042–17048.
- 8 T. Zhou, J. Shi, G. Li, B. Liu, B. Hu, G. Che, C. Liu, L. Wang and L. Yan, *J. Colloid Interface Sci.*, 2023, **632**, 285–298.
- 9 D. Cruz, J. Garcia Cerrillo, B. Kumru, N. Li, J. Dario Perea, B. V. K. J. Schmidt, I. Lauermaun, C. J. Brabec and M. Antonietti, *J. Am. Chem. Soc.*, 2019, **141**, 12322–12328.
- 10 C. Zhu, T. Wei, Y. Wei, L. Wang, M. Lu, Y. Yuan, L. Yin and L. Huang, *J. Mater. Chem. A*, 2021, **9**, 1207–1212.
- 11 T. Jordan, N. Fechler, J. Xu, T. J. K. Brenner, M. Antonietti and M. Shalom, *ChemCatChem*, 2015, **7**, 2826–2830.
- 12 C. Yang, B. Wang, L. Zhang, L. Yin and X. Wang, *Angew. Chem., Int. Ed.*, 2017, **56**, 6627–6631.
- 13 J. Shi, M. Tai, J. Hou, Y. Qiao, C. Liu, T. Zhou, L. Wang and B. Hu, *Chem. Eng. J.*, 2023, **456**, 141029.
- 14 Z.-A. Lan, G. Zhang and X. Wang, *Appl. Catal., B*, 2016, **192**, 116–125.
- 15 A. Gupta, T. Bhojar, B. M. Abraham, D. J. Kim, K. S. Pasupuleti, S. S. Umare, D. Vidyasagar and A. Gedanken, *ACS Appl. Mater. Interfaces*, 2023, **15**, 18898–18906.
- 16 G. Zhang, M. Zhang, X. Ye, X. Qiu, S. Lin and X. Wang, *Adv. Mater.*, 2014, **26**, 805–809.
- 17 Y. Wang, Y. Di, M. Antonietti, H. Li, X. Chen and X. Wang, *Chem. Mater.*, 2010, **22**, 5119–5121.
- 18 C. Liu, Y. Zhang, F. Dong, A. H. Reshak, L. Ye, N. Pinna, C. Zeng, T. Zhang and H. Huang, *Appl. Catal., B*, 2017, **203**, 465–474.
- 19 B. Zhu, J. Zhang, C. Jiang, B. Cheng and J. Yu, *Appl. Catal., B*, 2017, **207**, 27–34.
- 20 Q.-H. Zhu, Z. Chen, L.-N. Tang, Y. Zhong, X.-F. Zhao, L.-Z. Zhang and J.-H. Li, *Int. J. Hydrogen Energy*, 2019, **44**, 27704–27712.
- 21 T. Bhojar, N. Saraswat, M. V. Jyothirmai, A. Gupta, S. K. Malla, J. Park, D. Vidyasagar and S. S. Umare, *ACS Appl. Nano Mater.*, 2023, **6**, 3484–3496.
- 22 T. Bhojar, D. J. Kim, B. M. Abraham, A. Gupta, N. Maile, N. R. Manwar, S. Tonda, D. Vidyasagar and S. S. Umare, *iScience*, 2022, **25**, 105567.
- 23 P. E. Blöchl, *Phys. Rev. B: Condens. Matter Mater. Phys.*, 1994, **50**, 17953.
- 24 G. Kresse and J. Furthmüller, *Comput. Mater. Sci.*, 1996, **6**, 15–50.
- 25 J. P. Perdew, K. Burke and M. Ernzerhof, *Phys. Rev. Lett.*, 1996, **77**, 3865.
- 26 H. J. Monkhorst and J. D. Pack, *Phys. Rev. B: Condens. Matter Mater. Phys.*, 1976, **13**, 5188.
- 27 S. Grimme, *J. Comput. Chem.*, 2006, **27**, 1787–1799.
- 28 S. Grimme, *J. Comput. Chem.*, 2004, **25**, 1463–1473.
- 29 B. M. Abraham, *J. Phys. Chem. Solids*, 2021, **149**, 109777.
- 30 B. M. Abraham, *Mater. Today Commun.*, 2021, **26**, 101901.
- 31 S. Siahrostami, A. Verdager-Casadevall, M. Karamad, D. Deiana, P. Malacrida, B. Wickman, M. Escudero-Escribano, E. A. Paoli, R. Frydendal and T. W. Hansen, *Nat. Mater.*, 2013, **12**, 1137–1143.
- 32 A. Verdager-Casadevall, D. Deiana, M. Karamad, S. Siahrostami, P. Malacrida, T. W. Hansen, J. Rossmeisl, I. Chorkendorff and I. E. Stephens, *Nano Lett.*, 2014, **14**, 1603–1608.
- 33 T. Bhojar, D. Vidyasagar and S. S. Umare, *Mater. Today Commun.*, 2020, **24**, 101119.
- 34 Z. Li, Y. Zhou, Y. Zhou, K. Wang, Y. Yun, S. Chen, W. Jiao, L. Chen, B. Zou and M. Zhu, *Nat. Commun.*, 2023, **14**, 5742.
- 35 S. An, G. Zhang, K. Li, Z. Huang, X. Wang, Y. Guo, J. Hou, C. Song and X. Guo, *Adv. Mater.*, 2021, **33**, 2104361.
- 36 G. Zhang, A. Savateev, Y. Zhao, L. Li and M. Antonietti, *J. Mater. Chem. A*, 2017, **5**, 12723–12728.
- 37 D. Jang, S. Choi, N. H. Kwon, K. Y. Jang, S. Lee, T.-W. Lee, S.-J. Hwang, H. Kim, J. Kim and S. Park, *Appl. Catal., B*, 2022, **310**, 121313.
- 38 B. Zhai, H. Li, G. Gao, Y. Wang, P. Niu, S. Wang and L. Li, *Adv. Funct. Mater.*, 2022, 2207375.
- 39 X. Zhan, H. Wang, G. Zhou, L. Chen, Y. Sun, Y. Zhao, J. Liu and H. Shi, *ACS Appl. Mater. Interfaces*, 2021, **13**, 12118–12130.
- 40 M. Zhang, J. Wen, S. Zhang and Y. Zhai, *Sep. Purif. Technol.*, 2021, **257**, 117984.
- 41 Q. Gu, P. P. Jiang, Y. Shen, K. Zhang, P. T. Wai and A. Haryono, *Mol. Catal.*, 2021, **504**, 111441.
- 42 L. Chen, Y. Xu, Z. Yang, K. Zhang and B. Chen, *Appl. Catal., B*, 2020, **277**, 119207.
- 43 M. Wang, Y. Zeng, G. Dong and C. Wang, *Chin. J. Catal.*, 2020, **41**, 1498–1510.
- 44 L. Shen, G. Lei, Y. Zheng, S. Liang, F. Liu, S. Wang, Y. Cao, Y. Xiao and L. Jiang, *ChemCatChem*, 2021, **13**, 2386–2392.



- 45 J. Zheng, H.-T. Liu, B. Wu, C.-A. Di, Y.-L. Guo, T. Wu, G. Yu, Y.-Q. Liu and D.-B. Zhu, *Sci. Rep.*, 2012, **2**, 662.
- 46 T. Ishizaki, Y. Wada, S. Chiba, S. Kumagai, H. Lee, A. Serizawa, O. L. Li and G. Panomsuwan, *Phys. Chem. Chem. Phys.*, 2016, **18**, 21843–21851.
- 47 E. Prabakaran, T. Velempini, M. Molefe and K. Pillay, *J. Mater. Res. Technol.*, 2021, **15**, 6340–6355.
- 48 K. Liu, N. Zakharova, A. Adeyilola and L. Zeng, *Energy Fuels*, 2021, **35**, 2183–2191.
- 49 W. Wang, H. Zhang, S. Zhang, Y. Liu, G. Wang, C. Sun and H. Zhao, *Angew. Chem., Int. Ed.*, 2019, **58**, 16644–16650.
- 50 P. Xia, B. Cheng, J. Jiang and H. Tang, *Appl. Surf. Sci.*, 2019, **487**, 335–342.
- 51 J. Shao, H. Fei, H. Li, L. Yang, M. Li, J. Gao, H. Liao and J. Lu, *Sep. Purif. Technol.*, 2022, **297**, 121515.
- 52 J. Yan, J. Liu, Y. Sun, D. Ding, C. Wang, L. Sun and X. Li, *Inorg. Chem. Front.*, 2022, **9**, 1423–1433.
- 53 Y. Xie, Y. Dai, X. Yuan, L. Jiang, L. Zhou, Z. Wu, J. Zhang, H. Wang and T. Xiong, *J. Colloid Interface Sci.*, 2018, **530**, 493–504.
- 54 H. Guo, C.-G. Niu, X.-J. Wen, L. Zhang, C. Liang, X.-G. Zhang, D.-L. Guan, N. Tang and G.-M. Zeng, *J. Colloid Interface Sci.*, 2018, **513**, 852–865.
- 55 H. Wang, X. Yuan, Y. Wu, G. Zeng, W. Tu, C. Sheng, Y. Deng, F. Chen and J. W. Chew, *Appl. Catal., B*, 2017, **209**, 543–553.

